Journal of
Marine Science and Engineering

MDPI

Article

A Borehole Acoustic Calculation Approach with Gas Hydrate Saturation Inversion in Gas Hydrate-Bearing Sediments

Lin Liu [1,2], Xiumei Zhang [1,2,3,*] and Xiuming Wang [1,2,3]

[1] State Key Laboratory of Acoustics, Institute of Acoustics, Chinese Academy of Sciences, Beijing 100190, China; liulin@mail.ioa.ac.cn (L.L.); wangxm@mail.ioa.ac.cn (X.W.)
[2] Beijing Engineering Research Center of Sea Deep Drilling and Exploration, Institute of Acoustics, Chinese Academy of Sciences, Beijing 100190, China
[3] University of Chinese Academy of Sciences, Beijing 100049, China
* Correspondence: zhangxiumei@mail.ioa.ac.cn

Abstract: The inversion of gas hydrate saturation is a critical procedure in the evaluation of hydrate reservoirs. In this paper, a theoretical model for a borehole acoustic wavefield excited by multipole sources is established for the first time. On this basis, the attenuation of the dipole flexural waves is obtained, and in combination with the results of sensitivity analysis, an approach for inverting natural gas hydrates using the attenuation characteristics of the dipole flexural wave is proposed. The results of the sensitivity analysis demonstrate that the attenuation of the dipole flexural wave is sensitive to gas hydrate saturation. Numerical results derived from synthetic logging data are provided to illustrate the viability of the inversion of gas hydrate saturation. Even when significant noise is introduced into the receiver signal arrays, the inversion method remains stable and accurately assesses gas hydrate saturation. The correctness and effectiveness of the proposed approach are substantiated through the processing of numerical simulation data. This work provides a potent processing approach for evaluating reservoir hydrate saturation utilizing acoustic well-logging information.

Keywords: gas hydrate-bearing sediment; three-phase porous media; borehole acoustic wavefield; dipole flexural wave; gas hydrate saturation

Citation: Liu, L.; Zhang, X.; Wang, X. A Borehole Acoustic Calculation Approach with Gas Hydrate Saturation Inversion in Gas Hydrate-Bearing Sediments. *J. Mar. Sci. Eng.* **2024**, *12*, 271. https://doi.org/10.3390/jmse12020271

Academic Editor: Timothy S. Collett

Received: 12 January 2024
Revised: 29 January 2024
Accepted: 30 January 2024
Published: 1 February 2024

1. Introduction

In recent years, the focus of oil and gas exploration and development has transitioned from conventional reservoirs to complex unconventional ones [1,2]. The discovery of gas hydrates in permafrost regions of polar continental shelves and beneath seafloor sediments has piqued great interest. While opinions may vary regarding the concentration of gas hydrates in hydrate-bearing sediments and the overall methane content within gas hydrate accumulations, there is a consensus that the global methane reserves in gas hydrate deposits possess tremendous energy potential exceeding that of traditional oil, gas, and coal reserves [3–6]. Thus, gas hydrate epitomizes an unconventional energy asset poised to be significant in the forthcoming decades [7–13].

Geophysical well-logging is pivotal in pinpointing and quantifying gas hydrate reservoirs along with their constituents. The acoustic method is an important method of studying reservoir characteristics. Acoustic logging can proficiently measure the elastic parameters, porosity, and saturation of adjacent formations and is an indispensable technique for evaluating gas hydrate-bearing sediments. Gas hydrate-bearing sediments are three-phase porous media composed of a solid frame saturated with a fluid (usually water) and hydrates. The Carcione–Leclaire theory [14–16] is important for studying acoustic wave propagation in such a three-phase porous medium. The theory predicts three compressional and two shear waves produced when an acoustic wave propagates in a three-phase porous medium such as a gas hydrate-bearing sediment.

Currently, there is limited research on the acoustic wavefield within three-phase porous media in borehole environments. Due to the small difference between the compressional wave velocities of such a three-phase porous medium and the equivalent two-phase medium, scholars primarily utilize the compressional wave velocity obtained from acoustic logging to estimate the saturation of natural gas hydrates on the basis of the equivalent two-phase porous medium model. The saturation of gas hydrate in hydrate-bearing sediments was estimated by Shankar and Riedel using a combination of compressional wave velocity and resistivity logging [17]. Gao et al. [18] applied the improved Biot–Gassmann model proposed by Lee [19] to invert the saturation of gas hydrate in the hydrate-bearing reservoir using the acoustic wave velocity. Lin et al. [20] established a relationship between gas hydrate saturation and geological velocity based on the particle contact model [21] and the simplified three-phase equation [22]. Zhang et al. [23] studied the velocity dispersion and attenuation characteristics of acoustic waves in gas hydrate-bearing sediments using the effective medium theory [24] and used this model to predict the gas hydrate content in three drilling sites in the Shenhu area of the South China Sea. The authors of this paper [25] estimated gas hydrate saturation based on the velocity of the first kind of compressional wave of the Carcione–Leclaire three-phase Biot-type theory [26,27].

The aforementioned studies indicate that numerous scholars have researched the characteristics of gas hydrate reservoirs based on different models and utilized various models to estimate the hydrate saturation. The existence of gas hydrates essentially affects the physical properties of sediments. These alterations encompass key parameters such as permeability, porosity, and various geophysical characteristics including velocity, attenuation, and resistivity. [28]. Within these geophysical anomalies, the velocity and attenuation of both P- and S-waves have played a crucial role in characterizing the distribution and occurrence of hydrates. Furthermore, they have been instrumental in evaluating the hydrate saturation in gas hydrate-bearing sediments [29–33]. Logging curves exhibit large guide wave amplitudes, making them easy to identify, and they can, to some extent, reflect the reservoir's characteristics. However, the attenuation characteristics of guide waves in a borehole of three-phase porous media differ significantly from those in two-phase media. The lack of research on the borehole acoustic field of multiphase porous media hampers the effective utilization of guide wave information. The authors of this paper [34] studied the monopole borehole acoustic wavefield of a three-phase porous medium using the staggered-grid finite-difference time-domain (FDTD) scheme and the real axis integration (RAI) algorithm.

Due to the inability of traditional monopoles to receive shear head wave signals in slow formations, people usually use dipole sources to invert formation information [35–37]. This technology has not been limited to measuring only shear wave velocity but has also seen wider application and development. Its rapid development and extensive application are set to make significant contributions to hydrocarbon exploration in the field of acoustic logging. Currently, dipole acoustic logging is widely used in two-phase porous media. Nevertheless, the intricate nature of three-phase porous media poses significant challenges for research. Studies are scarce on the acoustic fields in a borehole and the responses elicited by multipole sources. This research gap hinders the potential application of multipole logging techniques for comprehensive reservoir evaluation.

In this paper, we present a representation approach for the borehole acoustic wavefield within three-phase porous media excited by multipole sources. Combining the acoustic potential function of the borehole and natural gas hydrate-bearing sediment with the boundary conditions of the borehole wall, the borehole acoustic waveforms can be obtained in the calculation. Further, the attenuation of the dipole flexural wave can be calculated. Building on this foundation, we propose an innovative methodology for estimating the saturation of natural gas hydrates in reservoirs using dipole flexural wave attenuation. The theoretical analysis investigates the sensitivity of the dipole flexural wave to gas hydrate saturation in a natural gas hydrate-bearing sediment (a three-phase porous medium). Based on this analysis, flexural wave attenuation is employed to inverse the saturation of

natural gas hydrates. The results demonstrate that this method can effectively estimate the saturation of natural gas hydrates.

2. Theoretical Model of the Borehole Acoustic Wavefield

Gas hydrate-bearing sediments represent a three-phase porous medium in which solid grains coexist with gas hydrates and water within the pore spaces. Drawing upon Biot's foundational theory, both Leclaire [14] and Carcione et al. [15] put forth a percolation theory, delving into the characteristics of acoustic wave propagation in such three-phase porous media. Their theory posits that, when an acoustic wave propagates in a three-phase porous medium, three compressional (P1, P2 and P3) and two shear (S1 and S2) waves are produced. Here, we delve into the analysis of the acoustic field within a borehole encompassed by such a porous medium.

The borehole wavefield in the frequency–wavenumber domain can be formulated as

$$\varphi(k_z,\omega) = \frac{iF}{n!\rho_f\omega^2}\left[\varepsilon_n K_n\left(\alpha_f r\right) + A_f(k_z,\omega) I_n\left(\alpha_f r\right)\right]\cos n(\theta-\theta_0), \tag{1}$$

where F symbolizes the frequency spectrum of the source. ε_n refers to the Neumann coefficient. The value of ε_n is equal to one when n is zero; when n is not zero, ε_n is equal to two. α_f pertains to the radial wavenumber associated with borehole fluid, r refers to the borehole radius, and A_f is an undetermined coefficient, interpreted as the reflection coefficient of the borehole wall. K_n and I_n are the modified Bessel functions, and the term "n" designates an n-th order sound source; in dipole acoustic logging, n = 1. In addition, $i = \sqrt{-1}$. The genuine time-domain waveform can be retrieved by employing a double Fourier transform. Both the dispersion and attenuation of mode waves hinge on the poles of $A_f(k_z,\omega)$ in the complex number domain.

In a three-phase porous medium, the acoustic wavefield is represented by the displacements of the solid grain frame $\vec{u}_1$, pore fluid $\vec{u}_2$, and gas hydrate $\vec{u}_3$. The displacements induced by monopole sources can be written as follows:

$$\begin{aligned}
\vec{u}_1 &= \nabla\varphi_1 + \nabla\times\nabla\times(\eta_1\hat{z}) + \nabla\times(\chi_1\hat{z}),\\
\vec{u}_2 &= \nabla\varphi_2 + \nabla\times\nabla\times(\eta_2\hat{z}) + \nabla\times(\chi_2\hat{z}),\\
\vec{u}_3 &= \nabla\varphi_3 + \nabla\times\nabla\times(\eta_3\hat{z}) + \nabla\times(\chi_3\hat{z}),
\end{aligned} \tag{2}$$

where φ_m, η_m, and χ_m (m = 1, 2, 3) denote the displacement potentials for compressional (P1, P2, and P3), SV (SV1, SV2) and SH (SH1 and SH2) waves, respectively. The displacement potentials for the compressional waves of each phase are segmented into three distinct parts, corresponding to the P1, P2, and P3 waves.

In the frequency–wavenumber domain, the displacement potentials for these compressional waves can be articulated as

$$\begin{aligned}
\varphi_1(r,k_z,\omega) &= \tfrac{iF}{2\rho_f\omega^2}[B_1(k_z,\omega)K_n(\alpha_{\mathrm{P}1}r) + C_1(k_z,\omega)K_n(\alpha_{\mathrm{P}2}r) + D_1(k_z,\omega)K_n(\alpha_{\mathrm{P}3}r)]\cos n(\theta-\theta_0),\\
\varphi_2(r,k_z,\omega) &= \tfrac{iF}{2\rho_f\omega^2}[B_2(k_z,\omega)K_n(\alpha_{\mathrm{P}1}r) + C_2(k_z,\omega)K_n(\alpha_{\mathrm{P}2}r) + D_2(k_z,\omega)K_n(\alpha_{\mathrm{P}3}r)]\cos n(\theta-\theta_0),\\
\varphi_3(r,k_z,\omega) &= \tfrac{iF}{2\rho_f\omega^2}[B_3(k_z,\omega)K_n(\alpha_{\mathrm{P}1}r) + C_3(k_z,\omega)K_n(\alpha_{\mathrm{P}2}r) + D_3(k_z,\omega)K_n(\alpha_{\mathrm{P}3}r)]\cos n(\theta-\theta_0),
\end{aligned} \tag{3}$$

where B_m, C_m, and D_m are the unknown amplitudes of three (one fast and two slow) compressional waves, respectively; $\alpha_{\mathrm{P}1}$, $\alpha_{\mathrm{P}2}$, and $\alpha_{\mathrm{P}3}$ are the radial wavenumbers of these compressional waves. In addition, the displacement potentials of SV waves in the frequency–wavenumber domain can be expressed as

$$\begin{aligned}\eta_1(r,k_z,\omega) &= \tfrac{iF}{2\rho_f\omega^2}[E_1(k_z,\omega)K_n(\alpha_{SV1}r)+F_1(k_z,\omega)K_n(\alpha_{SV2}r)]\cos n(\theta-\theta_0),\\ \eta_2(r,k_z,\omega) &= \tfrac{iF}{2\rho_f\omega^2}[E_2(k_z,\omega)K_n(\alpha_{SV1}r)+F_2(k_z,\omega)K_n(\alpha_{SV2}r)]\cos n(\theta-\theta_0),\\ \eta_3(r,k_z,\omega) &= \tfrac{iF}{2\rho_f\omega^2}[E_3(k_z,\omega)K_n(\alpha_{SV1}r)+F_3(k_z,\omega)K_n(\alpha_{SV2}r)]\cos n(\theta-\theta_0),\end{aligned} \tag{4}$$

where E_m and F_m represent two unknown amplitudes of the two kinds of SV waves, and α_{SV1} and α_{SV2} depict the radial wavenumbers corresponding to these SV waves. The displacement potentials of SH waves can be expressed as

$$\begin{aligned}\chi_1(r,k_z,\omega) &= \tfrac{iF}{2\rho_f\omega^2}[G_1(k_z,\omega)K_n(\alpha_{SH1}r)+H_1(k_z,\omega)K_n(\alpha_{SH2}r)]\sin n(\theta-\theta_0),\\ \chi_2(r,k_z,\omega) &= \tfrac{iF}{2\rho_f\omega^2}[G_2(k_z,\omega)K_n(\alpha_{SH1}r)+H_2(k_z,\omega)K_n(\alpha_{SH2}r)]\sin n(\theta-\theta_0),\\ \chi_3(r,k_z,\omega) &= \tfrac{iF}{2\rho_f\omega^2}[G_3(k_z,\omega)K_n(\alpha_{SH1}r)+H_3(k_z,\omega)K_n(\alpha_{SH2}r)]\sin n(\theta-\theta_0),\end{aligned} \tag{5}$$

where G_m and H_m represent two unknown amplitudes of the SH waves, while α_{SH1} and α_{SH2} depict the radial wavenumbers corresponding to these SH waves. Among the mentioned formulas, A_f, B_m, C_m, D_m, E_m, F_m, G_m, and H_m function as the undetermined coefficients. Their precise values are ascertained by adhering to the borehole wall's boundary conditions. Assuming a connection exists between the displacements of compressional waves for each phase:

$$\varphi_2 = l_1\varphi_1 = l_2\varphi_3, \tag{6}$$

subsequently, we can acquire

$$\begin{aligned}&B_2 = l_{11}B_1, C_2 = l_{12}C_1, D_2 = l_{13}D_1,\\ &B_3 = \tfrac{l_{11}}{l_{21}}B_1, C_3 = \tfrac{l_{12}}{l_{22}}C_1, D_3 = \tfrac{l_{13}}{l_{23}}D_1.\end{aligned} \tag{7}$$

Assuming a correlation exists between the displacements of SV waves for each phase:

$$\eta_2 = l_3\eta_1 = l_4\eta_3, \tag{8}$$

then we have

$$E_2 = l_{31}E_1,\ F_2 = l_{32}F_1,\ E_3 = \frac{l_{31}}{l_{41}}E_1,\ F_3 = \frac{l_{32}}{l_{42}}F_1. \tag{9}$$

Assuming a correlation exists between the displacement of SH waves for each phase:

$$\chi_2 = l_5\chi_1 = l_6\chi_3, \tag{10}$$

then we can get

$$G_2 = l_{51}G_1,\ H_2 = l_{52}H_1,\ G_3 = \frac{l_{51}}{l_{61}}G_1,\ \mathrm{H}_3 = \frac{l_{52}}{l_{62}}H_1. \tag{11}$$

The focus of this paper is on exploring the open-hole boundary conditions, which can be formulated as:

$$\begin{aligned}
&u_{rfin} = \phi_s u_{rs} + \phi_f u_{rf} + \phi_h u_{rh},\\
&-\phi_s P_{fin} = \sigma_{rrs},\\
&-\phi_h P_{fin} = \sigma_{rrh},\\
&P_{fin} = P_f,\\
&\tau_{rzs} = 0,\\
&\tau_{rzh} = 0,\\
&\tau_{r\theta s} = 0,\\
&\tau_{r\theta h} = 0,
\end{aligned} \tag{12}$$

where the subscripts *s*, *f*, and *h* correspond to solid grains, pore fluid, and hydrate, respectively. The subscripts *in* and *out* differentiate between the regions within and beyond the borehole wall. The first part of Equation (12) describes the continuous normal displacement of fluid both inside and outside the well. The next two equations indicate that the pressure of the fluid within the well, perpendicular to the borehole wall, is equal to the normal stress exerted by the solid grains and natural gas hydrates in the gas hydrate-bearing sediment. The fourth equation indicates that the pressure of the fluid within the well, in the vertical borehole direction, must be equivalent to the pressure of the fluid in the porous formation outside the well in that direction. The next two equations express the continuity of shear stresses in the *rz* direction. The seventh and eighth equations assert the continuity of shear stresses in the *rθ* direction. The specific expressions in the above equations can be expressed by

$$k_f = \frac{\omega}{v_f}, \tag{13}$$

$$\alpha_f = \sqrt{k_z^2 - k_f^2}, \tag{14}$$

$$\alpha_{\mathrm{Pi}} = \sqrt{k_z^2 - k_{\mathrm{Pi}}^2},\ \mathrm{i} = 1,\ 2,\ 3, \tag{15}$$

$$\alpha_{\mathrm{SVj}} = \sqrt{k_z^2 - k_{\mathrm{SVj}}^2},\ \mathrm{j} = 1,\ 2, \tag{16}$$

$$\alpha_{\mathrm{SHk}} = \sqrt{k_z^2 - k_{\mathrm{SHk}}^2},\ \mathrm{k} = 1,\ 2. \tag{17}$$

$$\alpha_{\mathrm{SHk}} = \sqrt{k_z^2 - k_{\mathrm{SHk}}^2},\ \mathrm{k} = 1,\ 2. \tag{18}$$

$$\begin{aligned}
\sigma_{rrs} = {} & \left(K_1 - \tfrac{2}{3}\mu_1\right)\left(-k_{\mathrm{P1}}^2 B_1 K_n(\alpha_{\mathrm{P1}}a) - k_{\mathrm{P2}}^2 C_1 K_n(\alpha_{\mathrm{P2}}a)\right.\\
&\left.-k_{\mathrm{P3}}^2 D_1 K_n(\alpha_{\mathrm{P3}}a)\right)\cos n(\theta-\theta_0) + C_{12}\left(-k_{\mathrm{P1}}^2 B_1 l_{11} K_n(\alpha_{\mathrm{P1}}a)\right.\\
&\left.-k_{\mathrm{P2}}^2 C_1 l_{12} K_n(\alpha_{\mathrm{P2}}a) - k_{\mathrm{P3}}^2 D_1 l_{13} K_n(\alpha_{\mathrm{P3}}a)\right)\cos n(\theta-\theta_0)\\
&+\left(C_{13} - \tfrac{1}{3}\mu_{13}\right)\left(-k_{\mathrm{P1}}^2 B_1 \tfrac{l_{11}}{l_{21}} K_n(\alpha_{\mathrm{P1}}a) - k_{\mathrm{P2}}^2 C_1 \tfrac{l_{12}}{l_{22}} K_n(\alpha_{\mathrm{P2}}a)\right.\\
&\left.-k_{\mathrm{P3}}^2 D_1 \tfrac{l_{13}}{l_{23}} K_n(\alpha_{\mathrm{P3}}a)\right)\cos n(\theta-\theta_0) + 2\mu_1 \tfrac{\partial \mu_{r1}}{\partial r} + \mu_{13}\tfrac{\partial \mu_{r3}}{\partial r},
\end{aligned} \tag{19}$$

$$\begin{aligned}
\sigma_f = {} & C_{12}\left(-k_{\mathrm{P1}}^2 B_1 K_n(\alpha_{\mathrm{P1}}a) - k_{\mathrm{P2}}^2 C_1 K_n(\alpha_{\mathrm{P2}}a)\right.\\
&\left.-k_{\mathrm{P3}}^2 D_1 K_n(\alpha_{\mathrm{P3}}a)\right)\cos n(\theta-\theta_0) + K_2\left(-k_{\mathrm{P1}}^2 B_1 l_{11} K_n(\alpha_{\mathrm{P1}}a)\right.\\
&\left.-k_{\mathrm{P2}}^2 C_1 l_{12} K_n(\alpha_{\mathrm{P2}}a) - k_{\mathrm{P3}}^2 D_1 l_{13} K_n(\alpha_{\mathrm{P3}}a)\right)\cos n(\theta-\theta_0)\\
&+\left(C_{23}\left(-k_{\mathrm{P1}}^2 B_1 \tfrac{l_{11}}{l_{21}} K_n(\alpha_{\mathrm{P1}}a) - k_{\mathrm{P2}}^2 C_1 \tfrac{l_{12}}{l_{22}} K_n(\alpha_{\mathrm{P2}}a)\right.\right.\\
&\left.\left.-k_{\mathrm{P3}}^2 D_1 \tfrac{l_{13}}{l_{23}} K_n(\alpha_{\mathrm{P3}}a)\right)\cos n(\theta-\theta_0),\right.
\end{aligned} \tag{20}$$

$$\begin{aligned}\sigma_{rrh} = &\left(C_{13} - \tfrac{1}{3}\mu_{13}\right)(-k_{\mathrm{P1}}^2 B_1 K_n(\alpha_{\mathrm{P1}}a) - k_{\mathrm{P2}}^2 C_1 K_n(\alpha_{\mathrm{P2}}a)\\ &-k_{\mathrm{P3}}^2 D_1 K_n(\alpha_{\mathrm{P3}}a))\cos n(\theta-\theta_0) + C_{23}(-k_{\mathrm{P1}}^2 B_1 l_{11} K_n(\alpha_{\mathrm{P1}}a)\\ &-k_{\mathrm{P2}}^2 C_1 l_{12} K_n(\alpha_{\mathrm{P2}}a) - k_{\mathrm{P3}}^2 D_1 l_{13} K_n(\alpha_{\mathrm{P3}}a))\cos n(\theta-\theta_0)\\ &+\left(K_3 - \tfrac{2}{3}\mu_{13}\right)(-k_{\mathrm{P1}}^2 B_1 \tfrac{l_{11}}{l_{21}} K_n(\alpha_{\mathrm{P1}}a) - k_{\mathrm{P2}}^2 C_1 \tfrac{l_{12}}{l_{22}} K_n(\alpha_{\mathrm{P2}}a)\\ &-k_{\mathrm{P3}}^2 D_1 \tfrac{l_{13}}{l_{23}} K_n(\alpha_{\mathrm{P3}}a))\cos n(\theta-\theta_0) + 2\mu_3 \tfrac{\partial \mu_{r1}}{\partial r} + \mu_{13}\tfrac{\partial \mu_{r3}}{\partial r},\end{aligned} \tag{21}$$

$$\sigma_{rzs} = \mu_1\left(\frac{\partial u_{rs}}{\partial z} + \frac{\partial u_{zs}}{\partial r}\right) + \frac{1}{2}\mu_{13}\left(\frac{\partial u_{rh}}{\partial z} + \frac{\partial u_{zh}}{\partial r}\right), \tag{22}$$

$$\sigma_{rzh} = \mu_3\left(\frac{\partial u_{rh}}{\partial z} + \frac{\partial u_{zs}}{\partial r}\right) + \frac{1}{2}\mu_{13}\left(\frac{\partial u_{rs}}{\partial z} + \frac{\partial u_{zs}}{\partial r}\right), \tag{23}$$

$$\sigma_{r\theta s} = \mu_1\left(\frac{\partial u_{\theta s}}{\partial r} - \frac{u_{\theta s}}{r} + \frac{1}{r}\frac{\partial u_{rs}}{\partial \theta}\right) + \frac{1}{2}\mu_{13}\left(\frac{\partial u_{\theta h}}{\partial r} - \frac{u_{\theta h}}{r} + \frac{1}{r}\frac{\partial u_{rh}}{\partial \theta}\right), \tag{24}$$

$$\sigma_{r\theta h} = \mu_3\left(\frac{\partial u_{\theta h}}{\partial r} - \frac{u_{\theta h}}{r} + \frac{1}{r}\frac{\partial u_{rh}}{\partial \theta}\right) + \frac{1}{2}\mu_{13}\left(\frac{\partial u_{\theta s}}{\partial r} - \frac{u_{\theta s}}{r} + \frac{1}{r}\frac{\partial u_{rs}}{\partial \theta}\right), \tag{25}$$

where K_1, K_2, and K_3 are the bulk moduli related to the solid grain, pore fluid, and gas hydrate; C_{12}, denotes the grain–fluid elastic coupling coefficient; C_{23} refers to the fluid–hydrate elastic coupling coefficient; and C_{13} represents the grain–hydrate elastic coupling coefficient.

The count of boundary conditions aligns with the number of undetermined coefficients both within and outside the well. By amalgamating the displacement derived from compressional and shear wave potentials with the boundary conditions specific to each phase, the ensuing linear equations can be formulated:

$$\begin{pmatrix} m_{11} & m_{12} & m_{13} & m_{14} & m_{15} & m_{16} & m_{17} & m_{18} \\ m_{21} & m_{22} & m_{23} & m_{24} & m_{25} & m_{26} & m_{27} & m_{28} \\ m_{31} & m_{32} & m_{33} & m_{34} & m_{35} & m_{36} & m_{37} & m_{38} \\ m_{41} & m_{42} & m_{43} & m_{44} & m_{45} & m_{46} & m_{47} & m_{48} \\ m_{51} & m_{52} & m_{53} & m_{54} & m_{55} & m_{56} & m_{57} & m_{58} \\ m_{61} & m_{62} & m_{63} & m_{64} & m_{65} & m_{66} & m_{67} & m_{68} \\ m_{71} & m_{72} & m_{73} & m_{74} & m_{75} & m_{76} & m_{77} & m_{78} \\ m_{81} & m_{82} & m_{83} & m_{84} & m_{85} & m_{86} & m_{87} & m_{88} \end{pmatrix} \begin{pmatrix} A_f \\ B_m \\ C_m \\ D_m \\ E_m \\ F_m \\ G_m \\ H_m \end{pmatrix} = \begin{pmatrix} b_1 \\ b_2 \\ b_3 \\ b_4 \\ 0 \\ 0 \\ 0 \\ 0 \end{pmatrix}, \tag{26}$$

By equating the determinant of the $\left[m_{ij}\right]_{8\times 8}$ to $D(k_z, \omega)$, and

$$N(k_z,\omega) = \begin{pmatrix} b_1 & m_{12} & m_{13} & m_{14} & m_{15} & m_{16} & m_{17} & m_{18} \\ b_2 & m_{22} & m_{23} & m_{24} & m_{25} & m_{26} & m_{27} & m_{28} \\ b_3 & m_{32} & m_{33} & m_{34} & m_{35} & m_{36} & m_{37} & m_{38} \\ b_4 & m_{42} & m_{43} & m_{44} & m_{45} & m_{46} & m_{47} & m_{48} \\ 0 & m_{52} & m_{53} & m_{54} & m_{55} & m_{56} & m_{57} & m_{58} \\ 0 & m_{62} & m_{63} & m_{64} & m_{65} & m_{66} & m_{67} & m_{68} \\ 0 & m_{72} & m_{73} & m_{74} & m_{75} & m_{76} & m_{77} & m_{78} \\ 0 & m_{82} & m_{83} & m_{84} & m_{85} & m_{86} & m_{87} & m_{88} \end{pmatrix}.$$

The borehole reflection coefficient A_f can be written as

$$A_f(k_z,\omega) = \frac{N(k_z,\omega)}{D(k_z,\omega)}. \tag{27}$$

By substituting Equation (27) into Equation (1), we can deduce the real waveform in the time domain by employing the Fourier transform. The expressions for m_{ij} (i, j = 1, 2, 3, 4, 5, 6, 7, 8) and b_i (i = 1, 2, 3, 4) are given in Appendix A.

3. Influence of Gas Hydrate Saturation on the Flexural Wave

The characteristics of the borehole wavefield are significantly influenced by reservoir parameters. Parameters like permeability and borehole characteristics notably impact the dipole flexural wave. In contrast to fluid-saturated porous media, the saturation of the pore solid in three-phase porous media remains a primary research focus. This is crucial for inverting the gas hydrate saturation. Yet, there is a noticeable gap in the research concerning the acoustic attributes of three-phase porous media and the impact of hydrate saturation on the characteristics of flexural waves. In our prior work, we introduced an approach centered on component waves, which integrates the branch-cut integral with the residue theorem, factoring in residues at leaky poles [38]. Sensitivity serves as a metric to highlight how a parameter affects the phase velocity and attenuation of waves across varying frequencies. In this section, we calculate the sensitivity of the flexural wave's phase velocity and attenuation to diverse parameters, aiming to discern the impact of these parameters on the flexural wave. The sensitivity is presented as [39]:

$$S_p(v) = \frac{p\partial v}{v\partial p},\ S_p(Q^{-1}) = \frac{p\partial Q^{-1}}{Q^{-1}\partial p}, \tag{28}$$

where S indicates the sensitivity, p represents the medium parameter, v signifies the velocity, and Q^{-1} refers to the attenuation. A sensitivity value greater than zero suggests that the characteristic increases with an increment in the variable, while a value less than zero implies a decrease.

Figure 1 shows the sensitivity of the attenuation of the flexural wave to hydrate saturation. The base value of the solid frame permeability $\kappa_{s0} = 1.07 \times 10^{-13}$ m^2 [14,15]. Porosities of 30–80% fundamentally cover the scope observed in hydrate-bearing sediments [28]; thus, the basic value of the porosity is chosen to be 0.5. The gas hydrate saturation is chosen to be 0.5, the pore fluid viscosity is 1.8×10^{-3} Pa·s [14–16,30], and the borehole fluid velocity is 1500 m/s. The physical parameters [14,15,30] are presented in Table 1, respectively. As can be observed from Figure 1, the flexural wave attenuation is sensitive to gas hydrate saturation, and the flexural wave attenuation decreases as the gas hydrate saturation increases.

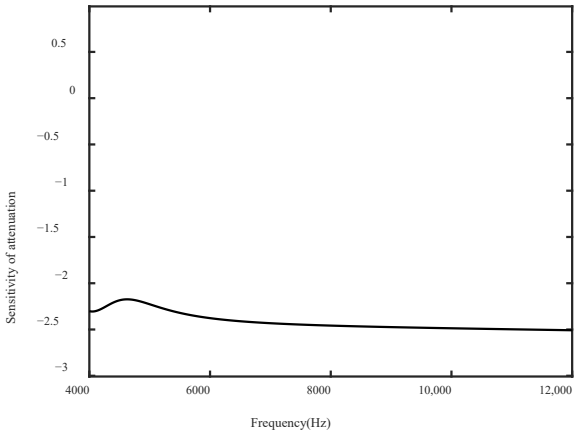

Figure 1. Sensitivity of the flexural wave attenuation to gas hydrate saturation. The base value of the solid frame permeability $\kappa_{s0} = 1.07 \times 10^{-13}$ m^2, the basic value of the porosity is chosen to be 0.5, the pore fluid viscosity is 1.8×10^{-3} Pa·s, and the borehole fluid velocity is 1500 m/s.

Table 1. Physical parameters of different phases [14,15,30].

Parameter	Value
Grain density (kg/m^3)	2650
Water density (kg/m^3)	1000

Table 1. *Cont.*

Parameter	Value
Gas hydrate density (kg/m^3)	900
Grain bulk modulus (GPa)	38.7
Grain shear modulus (GPa)	39.6
Water bulk modulus (GPa)	2.25
Gas hydrate bulk modulus (GPa)	8.58
Gas hydrate shear modulus (GPa)	3.32

4. The Inversion Method and Application to Field Data

Based on the sensitivity analysis of flexural wave attenuation, it can be seen that the gas hydrate saturation will have a certain influence on the flexural wave attenuation within a borehole of a gas hydrate-bearing sediment. Therefore, in this section, a method is proposed to invert the gas hydrate saturation by using flexural wave attenuation.

Assuming the amplitude of the mode wave is A_0 at a certain point, and the amplitude of the wave is A_1 after it has propagated L meters along the axis, then the relationship between the amplitude and the imaginary part of the pole wavenumber is given by

$$\frac{A_0}{LA_1} = \exp\left(\mathrm{Im}\left(k_{\mathrm{pole}}\right)\right). \tag{29}$$

As can be observed from the above equation, when the imaginary part is zero, $A_0 = A_1$, which means that the amplitude of the wave does not decay when propagating axially. When the imaginary part is not zero, $A_0 > A_1$, indicating that the amplitude of the wave decreases with axial propagation, and the larger the imaginary part value of the pole wavenumber, the faster the wave attenuation. In the field of acoustic instruments, decibel per meter (dB/m) is often used to define the attenuation, and the conversion relationship between the attenuation in dB/m and the imaginary part of the pole wavenumber is

$$\text{Attenuation in dB/m} = 20\log e^{\mathrm{Im}(k_{\mathrm{pole}})} = 8.686 \times \mathrm{Im}\left(k_{\mathrm{pole}}\right), \tag{30}$$

The inversion process can be achieved by minimizing the following objective function, constructed as the root-mean-square misfit error between the attenuation curve of the model and the measured attenuation data for the processing frequency range:

$$E(S_h) = \sum_{\Omega} ||\alpha_m(S_h;\omega) - \alpha_d(\omega)||^2, \tag{31}$$

where Ω is the frequency range of the calculated objective function, α_m denotes the attenuation curve calculated using the theoretical model, and α_d refers to the processed attenuation data, given by

$$\alpha_d(\omega) = \frac{1}{L}20\log[\frac{A_0(\omega)}{A_1(\omega)}], \tag{32}$$

and the Euclidean norm of the mismatch error can be used to simultaneously invert the gas hydrate saturation of the reservoir.

An example of a gas hydrate-bearing sediment proves that Equation (13) can be used to invert the gas hydrate saturation of the reservoir. Figure 2a,b show the borehole waveforms at distances of 2 m and 3 m, which are simulated by the staggered-grid finite-difference time-domain method in our previous work [34]. A rectangular window was used to intercept the flexural wave. Figure 3 represents the frequency spectrum of the flexural wave at a distance of 2 m and 3 m. The theoretical attenuation curve of α_m is obtained by changing the gas hydrate saturation of the reservoir; the parameters employed for calculating α_d are enumerated in Table 1. Figure 4 shows the inversion result calculated using the flexural

wave attenuation; the calculation frequency band Ω is chosen to be 5.35 kHz to 7.75 kHz. The gas hydrate saturation obtained by inversion is 0.492, with an error of 1.67%. Figure 5 shows the attenuation of the flexural wave of the theoretical calculation result and the processed attenuation data calculated by the simulated waveforms. As observed in Figure 5, in this frequency range, the theoretical calculation result is in good agreement with the processed attenuation data.

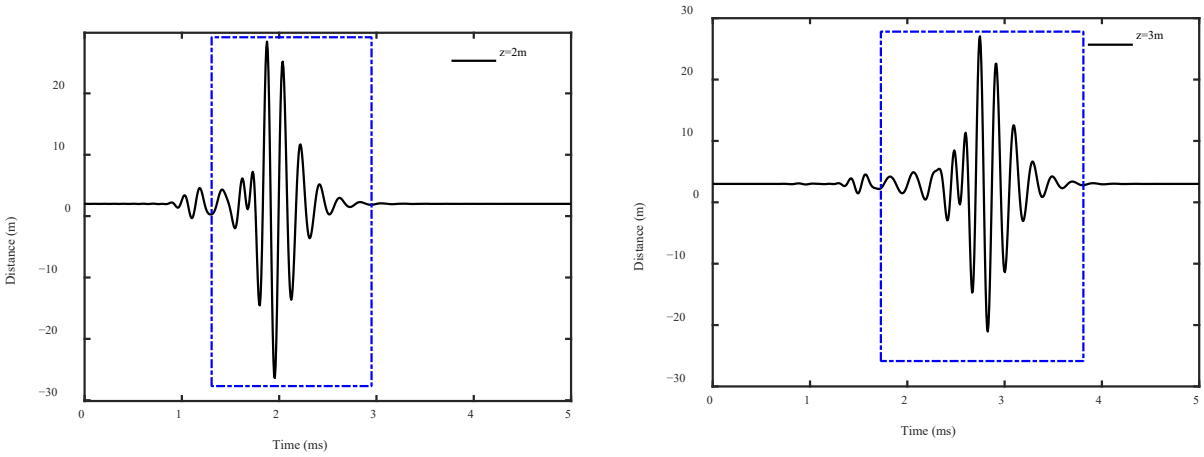

(**a**) (**b**)

Figure 2. The acoustic logging waveforms at a distance of (**a**) 2 m and (**b**) 3 m. The base value of the solid frame permeability $\kappa_{s0} = 1.07 \times 10^{-13}$ m^2, the basic value of the porosity is chosen to be 0.5, the gas hydrate saturation is chosen to be 0.5, the pore fluid viscosity is 1.8×10^{-3} Pa·s, and the borehole fluid velocity is 1500 m/s. The blue frame is the window for capturing the flexural wave.

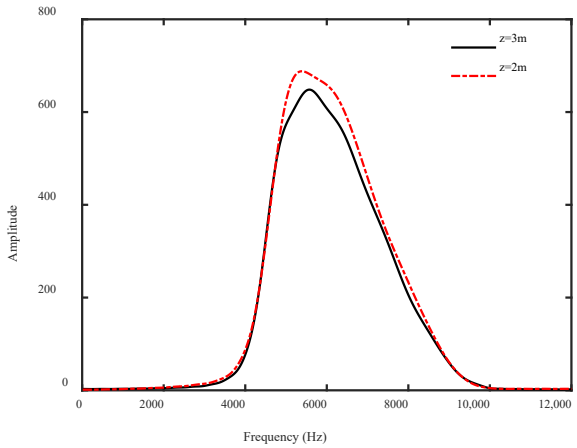

Figure 3. Frequency spectrum of waveforms of the flexural wave at distances of 2 m and 3 m. The black solid line represents the spectrum at a source distance of 3 m, and the red dotted line represents the spectrum at a source distance of 2 m.

To verify the reliability of this inversion method for signals with a signal-to-noise ratio (SNR), we artificially add noise to the data of the numerical simulation. Here, the low-frequency noise is processed by Gaussian noise through a low-pass filter in the 0–6.5 kHz frequency band. Each receiver is added with linearly independent noise signals, and the signal-to-noise ratio (SNR) is five. The central frequency of the monopole sources is selected as 6 kHz, and the borehole waveforms after adding noise are shown in Figure 6. It can be seen that noise seriously interferes with the waveforms. The waveform data after adding noise are used to invert the gas hydrate saturation by the inversion method proposed in this paper; the frequency spectrum is shown in Figure 7. As shown in Figure 8, after

adding noise, the inversion result of gas hydrate saturation is 0.495, and the error is 1%. Figure 9 shows a comparison between the attenuation of the theoretical calculation and the attenuation of the synthetic data.

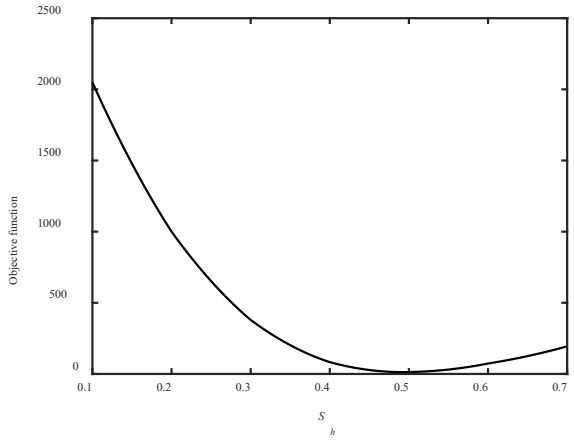

Figure 4. The inversion result of the gas hydrate saturation. The base value of the solid frame permeability $\kappa_{s0} = 1.07 \times 10^{-13}\text{m}^2$, the basic value of the porosity is chosen to be 0.5, the pore fluid viscosity is 1.8×10^{-3}Pa·s, and the borehole fluid velocity is 1500 m/s. The black solid line represents the variation of the objective function with natural gas hydrates, and the minimum value point is the inverted hydrate saturation.

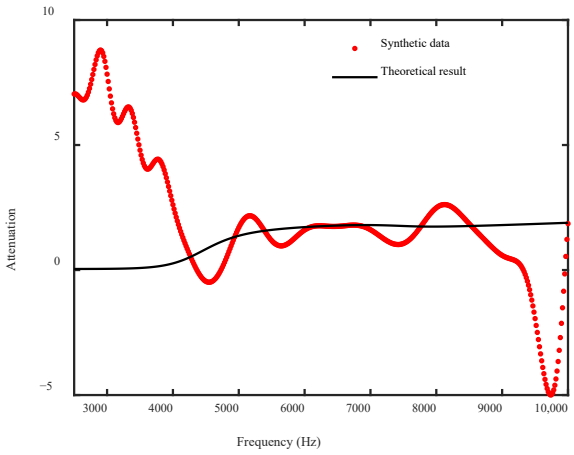

Figure 5. The attenuation of the flexural wave. The black solid line represents the theoretical calculation result, while the red dots are the processed attenuation data, which are obtained according to the waveforms of the flexural wave in the simulated full waveform.

To further verify the reliability of this inversion method for signals with a lower signal-to-noise ratio (SNR), we artificially add stronger noise to the data of numerical simulation. Here, the SNR is 3. The central frequency of the monopole sources is selected as 6 kHz, and the borehole waveforms after adding noise are shown in Figure 10. It can be seen that noise seriously interferes with the waveforms. The waveform data with added noise are used to invert the gas hydrate saturation by the inversion method proposed in this paper; the frequency spectrum is shown in Figure 11. As shown in Figure 12, after adding noise, the inversion result of gas hydrate saturation is 0.51, and the error is 2.33%. This result further proves the effectiveness of the inversion method. Figure 13 shows a comparison between the attenuation of the theoretical calculations and the attenuation of the processed data.

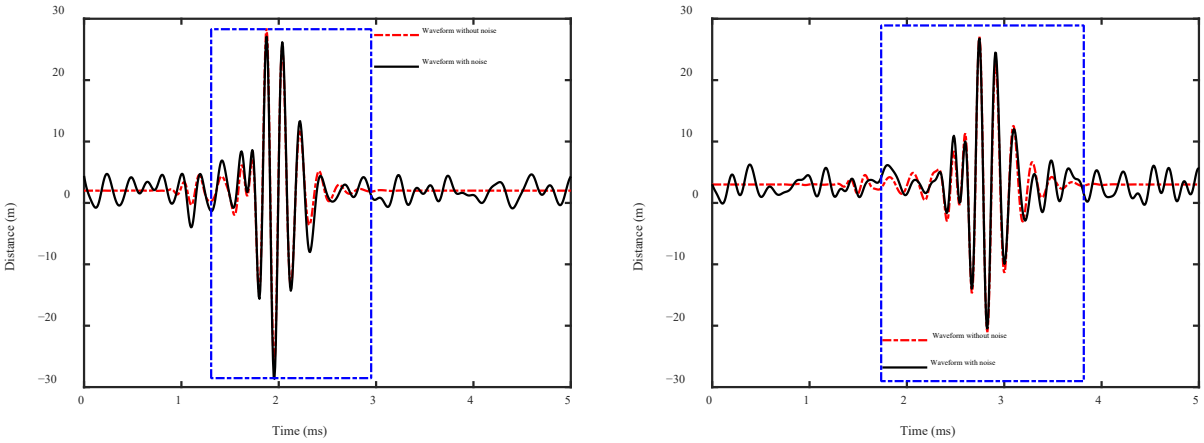

Figure 6. Waveforms after adding noise with an SNR of 5; the frequency is 6 kHz. The waveform data are used to obtain the attenuation data. (**a**) is the waveform at a distance of 2 m; (**b**) is the waveform at a distance of 3 m. The black solid line is the waveform with added noise, while the red dotted line is the waveform without added noise. The blue frame is the window for capturing the flexural wave.

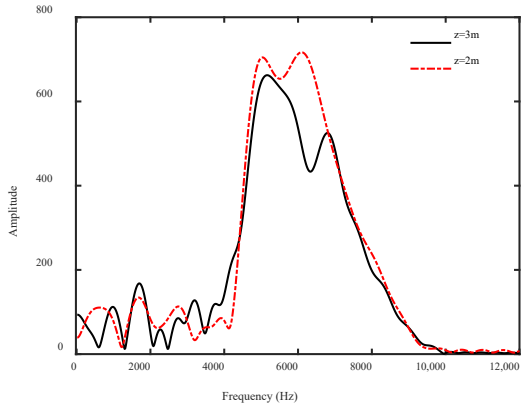

Figure 7. The frequency spectrum of waveforms of the flexural wave at distances of 2 m and 3 m with an SNR of 5. The black solid line represents the spectrum at a source distance of 3 m, and the red dotted line represents the spectrum at a source distance of 2 m.

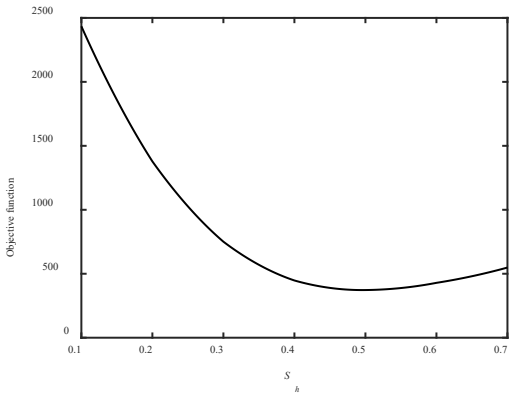

Figure 8. The detailed inversion result of the gas hydrate saturation with an SNR of 5. The base value of the solid frame permeability $\kappa_{s0} = 1.07 \times 10^{-13}$ m^2, the basic value of the porosity is chosen to be 0.5, the pore fluid viscosity is 1.8×10^{-3} Pa·s, and the borehole fluid velocity is 1500 m/s. The black solid line represents the variation of the objective function with natural gas hydrates, and the minimum value point is the inverted hydrate saturation.

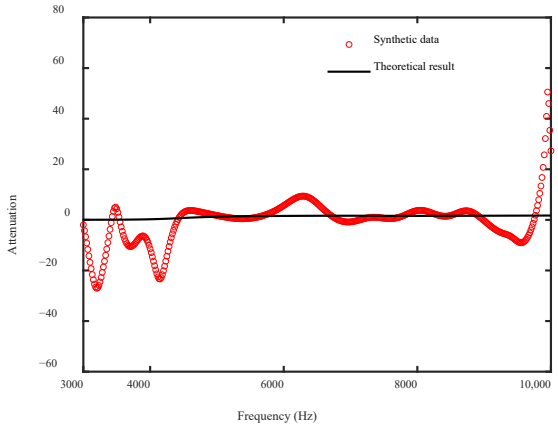

Figure 9. The attenuation of the flexural wave with an SNR of 5. The black solid line represents the theoretical calculation result, while the red dots are the processed data, which are obtained according to the synthetic waveforms of the flexural wave.

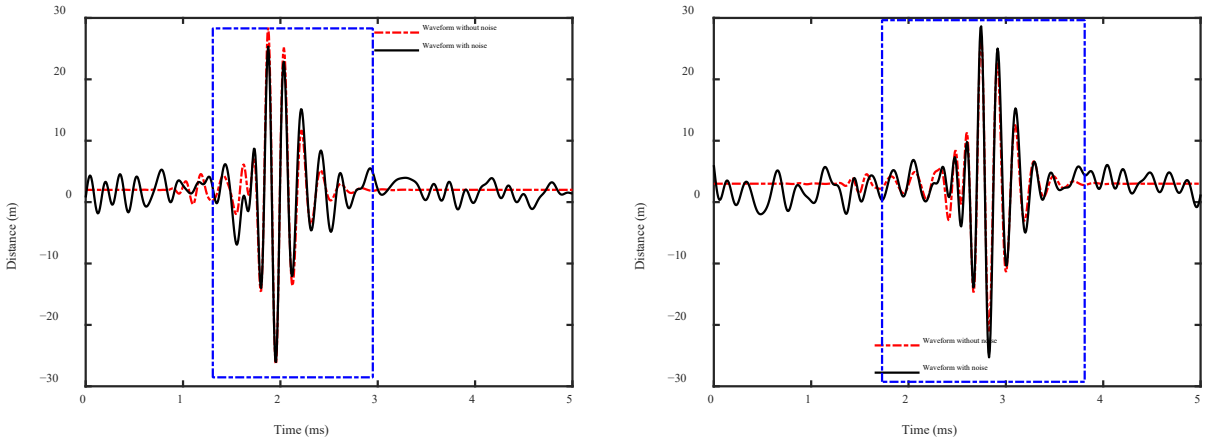

Figure 10. Waveforms after adding noise with an SNR of 3; the frequency is 6 kHz. The waveform data are used to obtain the attenuation data. (**a**) is the waveform at a distance of 2 m; (**b**) is the waveform at a distance of 3 m. The black solid line is the waveform with added noise, while the red dotted line is the waveform without added noise. The blue frame is the window for capturing the flexural wave.

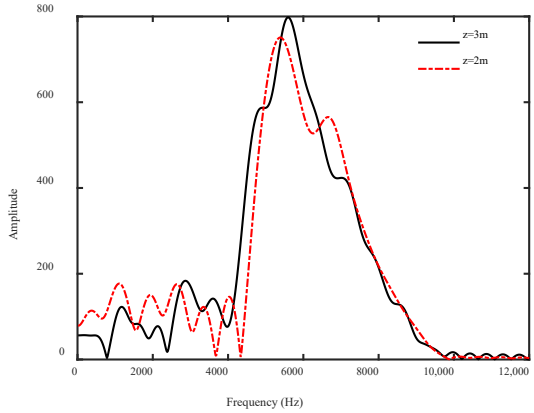

Figure 11. The frequency spectrum of waveforms of the flexural wave at a distance of 2 m and 3 m with an SNR of 3. The black solid line represents the spectrum at a source distance of 3 m, and the red dotted line represents the spectrum at a source distance of 2 m.

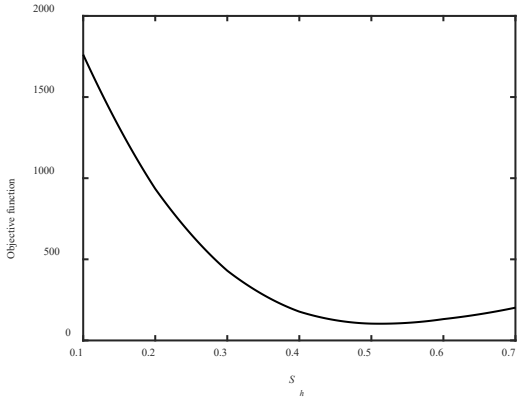

Figure 12. The detailed inversion result of the gas hydrate saturation with an SNR of 3. The base value of the solid frame permeability $\kappa_{s0} = 1.07 \times 10^{-13}$ m^2, the basic value of the porosity is chosen to be 0.5, the pore fluid viscosity is 1.8×10^{-3} Pa·s, and the borehole fluid velocity is 1500 m/s. The black solid line represents the variation of the objective function with natural gas hydrates, and the minimum value point is the inverted hydrate saturation.

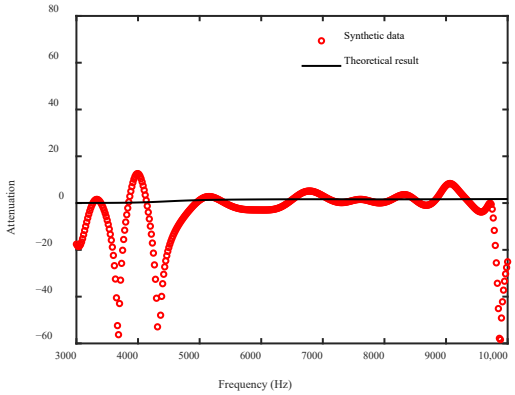

Figure 13. The attenuation of the flexural wave with an SNR of 3. The black solid line represents the theoretical calculation result, while the red dots are the processed data, which are obtained according to the synthetic waveforms of the flexural wave.

5. Conclusions

In this paper, based on the three-phase porous media theory, the borehole wavefield of a three-phase porous medium with multipole sources is calculated for the first time. The sensitivity of the flexural wave attenuation to gas hydrate saturation in a gas hydrate-bearing sediment is calculated and analyzed. A method using flexural wave attenuation to invert gas hydrate saturation is proposed. On this basis, the gas hydrate saturation of a gas hydrate-bearing sediment is estimated. The findings of our analysis are as follows.

(1) The attenuation of the flexural wave from dipole acoustic logging is sensitive to the gas hydrate saturation. Specifically, the attenuation of the flexural wave decreases with increasing hydrate saturation. The flexural wave attenuation can therefore be used to quantify the gas hydrate saturation.

(2) Based on the flexural wave analysis, we have developed an inversion method to simultaneously determine the gas hydrate saturation. We demonstrate that the attenuation of the flexural wave can effectively invert the gas hydrate saturation of natural gas hydrate-bearing sediments.

(3) In the inversion section, our research has some shortcomings. We have only theoretically demonstrated the feasibility of using dipole flexural waves to invert the saturation of natural gas hydrates, ignoring the complexity of the reservoir and the presence of logging tools that can have an impact on the results. In addition, real logging curves are often more complex than what we synthesized. However, we were unable to obtain

real on-site data, which prevented further analysis. Nevertheless, our research provides a theoretical foundation for the inversion of hydrate saturation using the attenuation of the flexural wave.

Author Contributions: L.L.: conceptualization, methodology, visualization, writing—original draft. X.Z.: conceptualization, methodology, writing—review and editing. X.W.: conceptualization, methodology, writing—review and editing. All authors have read and agreed to the published version of the manuscript.

Funding: This research was funded by the National Natural Science Foundation of China (Grant Nos. 12304496, 12334019, 11974018, 12274432, 52227901) and the Strategic Pilot and Technology Special of Chinese Academy of Sciences, China (Grant No. XDA14020303), and the Research Instrument and Equipment Development Project of Chinese Academy of Sciences-Key Technology Team Project (Grant No. GJJSTD20210008).

Institutional Review Board Statement: Not applicable.

Informed Consent Statement: Not applicable.

Data Availability Statement: Data are contained within the article.

Conflicts of Interest: The authors declare no conflict of interest.

Appendix A

$$
\begin{aligned}
m_{11} &= -\alpha_f I_{n+1}\left(\alpha_f a\right) - \left(n I_n\left(\alpha_f a\right)/a\right),\\
m_{12} &= ((nK_n(\alpha_{\mathrm{P1}}a) - \alpha_{\mathrm{P1}}aK_{n+1}(\alpha_{\mathrm{P1}}a))(\phi_h l_{11} + \phi_s l_{21} + \phi_w l_{11}l_{21}))/(l_{21}a),\\
m_{13} &= ((nK_n(\alpha_{\mathrm{P2}}a) - \alpha_{\mathrm{P2}}aK_{n+1}(\alpha_{\mathrm{P2}}a))(\phi_h l_{12} + \phi_s l_{22} + \phi_w l_{12}l_{22}))/(l_{22}a),\\
m_{14} &= ((nK_n(\alpha_{\mathrm{P3}}a) - \alpha_{\mathrm{P3}}aK_{n+1}(\alpha_{\mathrm{P3}}a))(\phi_h l_{13} + \phi_s l_{23} + \phi_w l_{13}l_{23}))/(l_{23}a),\\
m_{15} &= (k_z(nK_n(\alpha_{\mathrm{SV1}}a) - \alpha_{\mathrm{SV1}}K_{n+1}(\alpha_{\mathrm{SV1}}a))(\phi_h l_{31} + \phi_s l_{41} + \phi_w l_{31}l_{41})i)/(l_{41}a),\\
m_{16} &= (k_z(nK_n(\alpha_{\mathrm{SV2}}a) - \alpha_{\mathrm{SV2}}K_{n+1}(\alpha_{\mathrm{SV2}}a))(\phi_h l_{32} + \phi_s l_{42} + \phi_w l_{32}l_{42})i)/(l_{42}a),\\
m_{17} &= (nK_n(\alpha_{\mathrm{SH1}}a)(\phi_h l_{51} + \phi_s l_{61} + \phi_w l_{51}l_{61}))/(l_{61}a),\\
m_{18} &= (nK_n(\alpha_{\mathrm{SH2}}a)(\phi_h l_{52} + \phi_s l_{62} + \phi_w l_{52}l_{62}))/(l_{62}a),
\end{aligned}
\tag{A1}
$$

$$
\begin{aligned}
m_{21} &= \phi_s\rho_f\omega^2 I_n\left(\alpha_f a\right),\\
m_{22} &= (K_n(\alpha_{\mathrm{P1}}a)(6l_{21}\mu_1 n^2 + 3l_{11}\mu_{13}n^2 - 6l_{21}\mu_1 n - 3l_{11}\mu_{13}n - 3C_{13}k_{\mathrm{P1}}^2 l_{11}a^2\\
&-3K_1k_{\mathrm{P1}}^2 l_{21}a^2 + 2k_{\mathrm{P1}}^2 l_{21}\mu_1 a^2 + k_{\mathrm{P1}}^2 l_{11}\mu_{13}a^2 + 6l_{21}\mu_1\alpha_{\mathrm{P1}}^2 a^2 + 3l_{11}\mu_{13}\alpha_{\mathrm{P1}}^2 a^2\\
&-3C_{12}k_{\mathrm{P1}}^2 l_{11}l_{21}a^2))/\left(3l_{21}a^2\right) + (\alpha_{\mathrm{P1}}K_{n+1}(\alpha_{\mathrm{P1}}a)(2l_{21}\mu_1 + l_{11}\mu_{13}))/(l_{21}a),\\
m_{23} &= (K_n(\alpha_{\mathrm{P2}}a)(6l_{22}\mu_1 n^2 + 3l_{12}\mu_{13}n^2 - 6l_{22}\mu_1 n - 3l_{12}\mu_{13}n - 3C_{13}k_{\mathrm{P2}}^2 l_{12}a^2\\
&-3K_1k_{\mathrm{P2}}^2 l_{22}a^2 + 2k_{\mathrm{P2}}^2 l_{22}\mu_1 a^2 + k_{\mathrm{P2}}^2 l_{12}\mu_{13}a^2 + 6l_{22}\mu_1\alpha_{\mathrm{P2}}^2 a^2 + 3l_{12}\mu_{13}\alpha_{\mathrm{P2}}^2 a^2\\
&-3C_{12}k_{\mathrm{P2}}^2 l_{12}l_{22}a^2))/\left(3l_{22}a^2\right) + (\alpha_{\mathrm{P2}}K_{n+1}(\alpha_{\mathrm{P2}}a)(2l_{22}\mu_1 + l_{12}\mu_{13}))/(l_{22}a),\\
m_{24} &= (K_n(\alpha_{\mathrm{P3}}a)(6l_{23}\mu_1 n^2 + 3l_{13}\mu_{13}n^2 - 6l_{23}\mu_1 n - 3l_{13}\mu_{13}n - 3C_{13}k_{\mathrm{P3}}^2 l_{13}a^2\\
&-3K_1k_{\mathrm{P3}}^2 l_{23}a^2 + 2k_{\mathrm{P3}}^2 l_{23}\mu_1 a^2 + k_{\mathrm{P3}}^2 l_{13}\mu_{13}a^2 + 6l_{23}\mu_1\alpha_{\mathrm{P3}}^2 a^2 + 3l_{13}\mu_{13}\alpha_{\mathrm{P3}}^2 a^2\\
&-3C_{12}k_{\mathrm{P3}}^2 l_{13}l_{23}a^2))/\left(3l_{23}a^2\right) + (\alpha_{\mathrm{P3}}K_{n+1}(\alpha_{\mathrm{P3}}a)(2l_{23}\mu_1 + l_{13}\mu_{13}))/(l_{23}a),\\
m_{25} &= (k_z\alpha_{\mathrm{SV1}}K_{n+1}(\alpha_{\mathrm{SV1}}a)(2l_{41}\mu_1 i + l_{31}\mu_{13}i))/(l_{41}a)\\
&+(k_zK_n(\alpha_{\mathrm{SV1}}a)\left(2l_{41}\mu_1 + l_{31}\mu_{13}\left(\alpha_{\mathrm{SV1}}^2 a^2 + n^2 - n\right)i\right)/\left(l_{41}a^2\right),\\
m_{26} &= (k_z\alpha_{\mathrm{SV2}}K_{n+1}(\alpha_{\mathrm{SV2}}a)(2l_{42}\mu_1 i + l_{32}\mu_{13}i))/(l_{42}a)\\
&+(k_zK_n(\alpha_{\mathrm{SV2}}a)\left(2l_{42}\mu_1 + l_{32}\mu_{13}\left(\alpha_{\mathrm{SV2}}^2 a^2 + n^2 - n\right)i\right)/\left(l_{42}a^2\right),\\
m_{27} &= (nK_n(\alpha_{\mathrm{SH1}}a)(n-1)(2l_{61}\mu_1 + l_{51}\mu_{13}))/\left(l_{61}a^2\right)\\
&-(\alpha_{\mathrm{SH1}}nK_{n+1}(\alpha_{\mathrm{SH1}}a)(2l_{61}\mu_1 + l_{51}\mu_{13}))/(l_{61}a),\\
m_{28} &= (nK_n(\alpha_{\mathrm{SH2}}a)(n-1)(2l_{62}\mu_1 + l_{52}\mu_{13}))/\left(l_{62}a^2\right)\\
&-(\alpha_{\mathrm{SH2}}nK_{n+1}(\alpha_{\mathrm{SH2}}a)(2l_{62}\mu_1 + l_{52}\mu_{13}))/(l_{62}a),
\end{aligned}
\tag{A2}
$$

$$
\begin{aligned}
&m_{31} = \phi_w \rho_f \omega^2 I_n\left(\alpha_f a\right),\\
&m_{32} = -C_{12}k_{\mathrm{P1}}^2 K_n(\alpha_{\mathrm{P1}}a) - K_2 k_{\mathrm{P1}}^2 l_{11} K_n(\alpha_{\mathrm{P1}}a) - \left(C_{23}k_{\mathrm{P1}}^2 l_{11} K_n(\alpha_{\mathrm{P1}}a)\right)/l_{21},\\
&m_{33} = -C_{12}k_{\mathrm{P2}}^2 K_n(\alpha_{\mathrm{P2}}a) - K_2 k_{\mathrm{P2}}^2 l_{12} K_n(\alpha_{\mathrm{P2}}a) - \left(C_{23}k_{\mathrm{P2}}^2 l_{12} K_n(\alpha_{\mathrm{P2}}a)\right)/l_{22},\\
&m_{34} = -C_{12}k_{\mathrm{P3}}^2 K_n(\alpha_{\mathrm{P3}}a) - K_2 k_{\mathrm{P3}}^2 l_{13} K_n(\alpha_{\mathrm{P3}}a) - \left(C_{23}k_{\mathrm{P3}}^2 l_{13} K_n(\alpha_{\mathrm{P3}}a)\right)/l_{23},\\
&m_{35} = 0,\\
&m_{36} = 0,\\
&m_{37} = 0,\\
&m_{38} = 0,
\end{aligned}
\tag{A3}
$$

$$
\begin{aligned}
&m_{41} = \phi_h \rho_f \omega^2 I_n\left(\alpha_f a\right),\\
&m_{42} = (K_n(\alpha_{\mathrm{P1}}a)(6l_{11}\mu_3 n^2 + 3l_{21}\mu_{13}n^2 - 6l_{11}\mu_3 n - 3l_{21}\mu_{13}n - 3C_{13}k_{\mathrm{P1}}^2 l_{21}a^2\\
&-3K_3 k_{\mathrm{P1}}^2 l_{11}a^2 + 2k_{\mathrm{P1}}^2 l_{11}\mu_{13}a^2 + k_{P1}^2 l_{21}\mu_{13}a^2 + 6l_{11}\mu_3\alpha_{\mathrm{P1}}^2 a^2 + 3l_{21}\mu_{13}\alpha_{\mathrm{P1}}^2 a^2\\
&-3C_{23}k_{\mathrm{P1}}^2 l_{11}l_{21}a^2))/\left(3l_{21}a^2\right) + (\alpha_{\mathrm{P1}}K_{n+1}(\alpha_{\mathrm{P1}}a)(2l_{11}\mu_3 + l_{21}\mu_{13}))/(l_{21}a),\\
&m_{43} = (K_n(\alpha_{\mathrm{P2}}a)(6l_{12}\mu_3 n^2 + 3l_{22}\mu_{13}n^2 - 6l_{12}\mu_3 n - 3l_{22}\mu_{13}n - 3C_{13}k_{\mathrm{P2}}^2 l_{22}a^2\\
&-3K_3 k_{\mathrm{P2}}^2 l_{12}a^2 + 2k_{\mathrm{P2}}^2 l_{12}\mu_{13}a^2 + k_{\mathrm{P2}}^2 l_{22}\mu_{13}a^2 + 6l_{12}\mu_3\alpha_{\mathrm{P2}}^2 a^2 + 3l_{22}\mu_{13}\alpha_{\mathrm{P2}}^2 a^2\\
&-3C_{23}k_{\mathrm{P2}}^2 l_{12}l_{22}a^2))/\left(3l_{22}a^2\right) + (\alpha_{\mathrm{P2}}K_{n+1}(\alpha_{\mathrm{P2}}a)(2l_{12}\mu_3 + l_{22}\mu_{13}))/(l_{22}a),\\
&m_{44} = (K_n(\alpha_{\mathrm{P3}}a)(6l_{13}\mu_3 n^2 + 3l_{23}\mu_{13}n^2 - 6l_{13}\mu_3 n - 3l_{23}\mu_{13}n - 3C_{13}k_{\mathrm{P3}}^2 l_{23}a^2\\
&-3K_3 k_{\mathrm{P3}}^2 l_{13}a^2 + 2k_{\mathrm{P3}}^2 l_{13}\mu_{13}a^2 + k_{\mathrm{P3}}^2 l_{23}\mu_{13}a^2 + 6l_{13}\mu_3\alpha_{\mathrm{P3}}^2 a^2 + 3l_{23}\mu_{13}\alpha_{\mathrm{P3}}^2 a^2\\
&-3C_{23}k_{\mathrm{P3}}^2 l_{13}l_{23}a^2))/\left(3l_{23}a^2\right) + (\alpha_{\mathrm{P3}}K_{n+1}(\alpha_{\mathrm{P3}}a)(2l_{13}\mu_3 + l_{23}\mu_{13}))/(l_{23}a),\\
&m_{25} = (k_z\alpha_{\mathrm{SV1}}K_{n+1}(\alpha_{\mathrm{SV1}}a)(2l_{31}\mu_3 i + l_{41}\mu_{13}i))/(l_{41}a)\\
&+(k_z K_n(\alpha_{\mathrm{SV1}}a)\left(2l_{31}\mu_3 + l_{41}\mu_{13}\left(\alpha_{\mathrm{SV1}}^2 a^2 + n^2 - n\right)i\right)/\left(l_{41}a^2\right),\\
&m_{46} = (k_z\alpha_{\mathrm{SV2}}K_{n+1}(\alpha_{\mathrm{SV2}}a)(2l_{32}\mu_3 i + l_{42}\mu_{13}i))/(l_{42}a)\\
&+(k_z K_n(\alpha_{\mathrm{SV2}}a)\left(2l_{32}\mu_3 + l_{42}\mu_{13}\left(\alpha_{\mathrm{SV2}}^2 a^2 + n^2 - n\right)i\right)/\left(l_{42}a^2\right),\\
&m_{47} = (nK_n(\alpha_{\mathrm{SH1}}a)(n-1)(2l_{51}\mu_3 + l_{61}\mu_{13}))/\left(l_{61}a^2\right)\\
&-(\alpha_{\mathrm{SH1}}nK_{n+1}(\alpha_{\mathrm{SH1}}a)(2l_{51}\mu_3 + l_{61}\mu_{13}))/(l_{61}a),\\
&m_{48} = (nK_n(\alpha_{\mathrm{SH2}}a)(n-1)(2l_{52}\mu_3 + l_{62}\mu_{13}))/\left(l_{62}a^2\right)\\
&-(\alpha_{\mathrm{SH2}}nK_{n+1}(\alpha_{\mathrm{SH2}}a)(2l_{52}\mu_3 + l_{62}\mu_{13}))/(l_{62}a),
\end{aligned}
\tag{A4}
$$

$$
\begin{aligned}
&m_{51} = 0,\\
&m_{52} = (k_z(2l_{21}\mu_1 + l_{11}\mu_{13})(nK_n(\alpha_{\mathrm{P1}}a) - \alpha_{\mathrm{P1}}aK_{n+1}(\alpha_{\mathrm{P1}}a))i/(l_{21}a),\\
&m_{53} = (k_z(2l_{22}\mu_1 + l_{12}\mu_{13})(nK_n(\alpha_{\mathrm{P2}}a) - \alpha_{\mathrm{P2}}aK_{n+1}(\alpha_{\mathrm{P2}}a))i/(l_{22}a),\\
&m_{54} = (k_z(2l_{23}\mu_1 + l_{13}\mu_{13})(nK_n(\alpha_{\mathrm{P3}}a) - \alpha_{\mathrm{P3}}aK_{n+1}(\alpha_{\mathrm{P3}}a))i/(l_{23}a),\\
&m_{55} = \left(\left(k_{\mathrm{SV1}}^2 - 2k_z^2\right)(2l_{41}\mu_1 + l_{31}\mu_{13})(nK_n(\alpha_{\mathrm{SV1}}a) - \alpha_{\mathrm{SV1}}aK_{n+1}(\alpha_{\mathrm{SV1}}a))\right)/(2l_{41}a),\\
&m_{56} = \left(\left(k_{\mathrm{SV2}}^2 - 2k_z^2\right)(2l_{42}\mu_1 + l_{32}\mu_{13})(nK_n(\alpha_{\mathrm{SV2}}a) - \alpha_{\mathrm{SV2}}aK_{n+1}(\alpha_{\mathrm{SV2}}a))\right)/(2l_{42}a),\\
&m_{57} = (k_z nK_n(\alpha_{\mathrm{SH1}}a)(2l_{61}\mu_1 i + l_{51}\mu_{13}i))/(2l_{61}a),\\
&m_{58} = (k_z nK_n(\alpha_{\mathrm{SH2}}a)(2l_{62}\mu_1 i + l_{52}\mu_{13}i))/(2l_{62}a),
\end{aligned}
\tag{A5}
$$

$$
\begin{aligned}
&m_{61} = 0,\\
&m_{62} = (k_z(2l_{11}\mu_3 + l_{21}\mu_{13})(nK_n(\alpha_{\mathrm{P1}}a) - \alpha_{\mathrm{P1}}aK_{n+1}(\alpha_{\mathrm{P1}}a))i/(l_{21}a),\\
&m_{63} = (k_z(2l_{12}\mu_3 + l_{22}\mu_{13})(nK_n(\alpha_{\mathrm{P2}}a) - \alpha_{\mathrm{P2}}aK_{n+1}(\alpha_{\mathrm{P2}}a))i/(l_{22}a),\\
&m_{64} = (k_z(2l_{13}\mu_3 + l_{23}\mu_{13})(nK_n(\alpha_{\mathrm{P3}}a) - \alpha_{\mathrm{P3}}aK_{n+1}(\alpha_{\mathrm{P3}}a))i/(l_{23}a),\\
&m_{65} = \left(\left(k_{\mathrm{SV1}}^2 - 2k_z^2\right)(2l_{31}\mu_3 + l_{41}\mu_{13})(nK_n(\alpha_{\mathrm{SV1}}a) - \alpha_{\mathrm{SV1}}aK_{n+1}(\alpha_{\mathrm{SV1}}a))\right)/(2l_{41}a),\\
&m_{66} = \left(\left(k_{\mathrm{SV2}}^2 - 2k_z^2\right)(2l_{32}\mu_3 + l_{42}\mu_{13})(nK_n(\alpha_{\mathrm{SV2}}a) - \alpha_{\mathrm{SV2}}aK_{n+1}(\alpha_{\mathrm{SV2}}a))\right)/(2l_{42}a),\\
&m_{67} = (k_z nK_n(\alpha_{\mathrm{SH1}}a)(2l_{51}\mu_3 i + l_{61}\mu_{13}i))/(2l_{61}a),\\
&m_{68} = (k_z nK_n(\alpha_{\mathrm{SH2}}a)(2l_{52}\mu_1 i + l_{62}\mu_{13}i))/(2l_{62}a),
\end{aligned}
\tag{A6}
$$

$$
\begin{aligned}
&m_{71} = 0,\\
&m_{72} = (nK_n(\alpha_{P1}a)(n-1)(2l_{21}\mu_1 + l_{11}\mu_{13}))/(l_{21}a^2)\\
&-(\alpha_{P1}nK_{n+1}(\alpha_{P1}a)(2l_{21}\mu_1 + l_{11}\mu_{13}))/(l_{21}a),\\
&m_{73} = (nK_n(\alpha_{P2}a)(n-1)(2l_{22}\mu_1 + l_{12}\mu_{13}))/(l_{22}a^2)\\
&-(\alpha_{P2}nK_{n+1}(\alpha_{P2}a)(2l_{22}\mu_1 + l_{12}\mu_{13}))/(l_{22}a),\\
&m_{74} = (nK_n(\alpha_{P3}a)(n-1)(2l_{23}\mu_1 + l_{13}\mu_{13}))/(l_{23}a^2)\\
&-(\alpha_{P3}nK_{n+1}(\alpha_{P3}a)(2l_{23}\mu_1 + l_{13}\mu_{13}))/(l_{23}a),\\
&m_{75} = -(k_z\alpha_{SV1}nK_{n+1}(\alpha_{SV1}a)(2l_{41}\mu_1 i + l_{31}\mu_{13}i))/(l_{41}a)\\
&+(k_z nK_n(\alpha_{SV1}a)(n-1)(2l_{41}\mu_1 + l_{31}\mu_{13})i)/(l_{41}a^2),\\
&m_{76} = -(k_z\alpha_{SV2}nK_{n+1}(\alpha_{SV2}a)(2l_{42}\mu_1 i + l_{32}\mu_{13}i))/(l_{42}a)\\
&+(k_z nK_n(\alpha_{SV2}a)(n-1)(2l_{42}\mu_1 + l_{32}\mu_{13})i)/(l_{42}a^2),\\
&m_{77} = K_n(\alpha_{SH1}a)(2l_{61}\mu_1 + l_{51}\mu_{13})(\alpha_{SH1}^2a^2 + 2n^2 - 2n))/(2l_{61}a^2)\\
&+\alpha_{SH1}K_{n+1}(\alpha_{SH1}a)(2l_{61}\mu_1 + l_{51}\mu_{13}))/(l_{61}a),\\
&m_{78} = K_n(\alpha_{SH2}a)(2l_{62}\mu_1 + l_{52}\mu_{13})(\alpha_{SH2}^2a^2 + 2n^2 - 2n))/(2l_{62}a^2)\\
&+\alpha_{SH2}K_{n+1}(\alpha_{SH2}a)(2l_{62}\mu_1 + l_{52}\mu_{13}))/(l_{62}a),
\end{aligned}
\tag{A7}
$$

$$
\begin{aligned}
&m_{81} = 0,\\
&m_{82} = (nK_n(\alpha_{P1}a)(n-1)(2l_{11}\mu_3 + l_{21}\mu_{13}))/(l_{21}a^2)\\
&-(\alpha_{P1}nK_{n+1}(\alpha_{P1}a)(2l_{11}\mu_3 + l_{21}\mu_{13}))/(l_{21}a),\\
&m_{83} = (nK_n(\alpha_{P2}a)(n-1)(2l_{12}\mu_3 + l_{22}\mu_{13}))/(l_{22}a^2)\\
&-(\alpha_{P2}nK_{n+1}(\alpha_{P2}a)(2l_{12}\mu_3 + l_{22}\mu_{13}))/(l_{22}a),\\
&m_{84} = (nK_n(\alpha_{P3}a)(n-1)(2l_{13}\mu_3 + l_{23}\mu_{13}))/(l_{23}a^2)\\
&-(\alpha_{P3}nK_{n+1}(\alpha_{P3}a)(2l_{13}\mu_3 + l_{23}\mu_{13}))/(l_{23}a),\\
&m_{85} = -(k_z\alpha_{SV1}nK_{n+1}(\alpha_{SV1}a)(2l_{31}\mu_3 i + l_{41}\mu_{13}i))/(l_{41}a)\\
&+(k_z nK_n(\alpha_{SV1}a)(n-1)(2l_{31}\mu_3 + l_{41}\mu_{13})i)/(l_{41}a^2),\\
&m_{86} = -(k_z\alpha_{SV2}nK_{n+1}(\alpha_{SV2}a)(2l_{32}\mu_3 i + l_{42}\mu_{13}i))/(l_{42}a)\\
&+(k_z nK_n(\alpha_{SV2}a)(n-1)(2l_{32}\mu_3 + l_{42}\mu_{13})i)/(l_{42}a^2),\\
&m_{87} = K_n(\alpha_{SH1}a)(2l_{51}\mu_3 + l_{61}\mu_{13})(\alpha_{SH1}^2a^2 + 2n^2 - 2n))/(2l_{61}a^2)\\
&+\alpha_{SH1}K_{n+1}(\alpha_{SH1}a)(2l_{51}\mu_3 + l_{61}\mu_{13}))/(l_{61}a),\\
&m_{88} = K_n(\alpha_{SH2}a)(2l_{52}\mu_3 + l_{62}\mu_{13})(\alpha_{SH2}^2a^2 + 2n^2 - 2n))/(2l_{62}a^2)\\
&+\alpha_{SH2}K_{n+1}(\alpha_{SH2}a)(2l_{52}\mu_3 + l_{62}\mu_{13}))/(l_{62}a),
\end{aligned}
\tag{A8}
$$

$$
\begin{aligned}
b_1 &= -2\alpha_f K_{n+1}(\alpha_f a) + 2(nK_n(\alpha_f a))/a,\\
b_2 &= -2\phi_s\rho_f\omega^2 K_n(\alpha_f a),\\
b_3 &= -2\phi_w\rho_f\omega^2 K_n(\alpha_f a),\\
b_4 &= -2\phi_h\rho_f\omega^2 K_n(\alpha_f a),\\
b_5 &= 0,\\
b_6 &= 0,\\
b_7 &= 0,\\
b_8 &= 0.
\end{aligned}
\tag{A9}
$$

References

1. Farahani, M.V.; Hassanpouryouzband, A.; Yang, J.; Tohidi, B. Development of a coupled geophysical-geothermal scheme for quantification of hydrates in gas hydrate-bearing permafrost sediments. *Phys. Chem. Chem. Phys.* **2021**, *23*, 24249–24264. [CrossRef]
2. Farahani, M.V.; Hassanpouryouzband, A.; Yang, J.; Tohidi, B. Insights into the climate-driven evolution of gas hydrate-bearing permafrost sediments: Implications for prediction of environmental impacts and security of energy in cold regions. *RSC Adv.* **2021**, *11*, 14334–14346. [CrossRef]

3. Demirbas, A. Methane hydrates as potential energy resource: Part 2—Methane production processes from gas hydrates. *Energy Convers. Manag.* **2010**, *51*, 1562–1571. [CrossRef]
4. Demirbas, A.; Rehan, M.; Al-Sasi, B.O.; Nizami, A.S. Evaluation of natural gas hydrates as a future methane source. *Pet. Sci. Technol.* **2016**, *34*, 1204–1210. [CrossRef]
5. Swaranjit Singh, A.A. Natural gas hydrate as an upcoming resource of energy. *J. Pet. Environ. Biotechnol.* **2015**, *6*, 16. [CrossRef]
6. Dawe, R.A.; Thomas, S. A large potential methane source-natural gas hydrates. *Energy Sources Part A Recover. Util. Environ. Eff.* **2007**, *29*, 217–229. [CrossRef]
7. Hassanpouryouzband, A.; Joonaki, E.; Vasheghani Farahani, M.; Takeya, S.; Ruppel, C.; Yang, J.; English, N.J.; Schicks, J.M.; Edlmann, K.; Mehrabian, H.; et al. Gas hydrates in sustainable chemistry. *Chem. Soc. Rev.* **2020**, *49*, 5225–5309. [CrossRef]
8. Kelland, M. Natural gas hydrates: Energy for the future. *Mar. Pollut. Bull.* **1994**, *29*, 307–311. [CrossRef]
9. Minshull, T.A.; Marín-Moreno, H.; Betlem, P.; Bialas, J.; Bünz, S.; Burwicz, E.; Cameselle, A.L.; Cifci, G.; Giustiniani, M.; Hillman, J.I.T.; et al. Hydrate occurrence in Europe: A review of available evidence. *Mar. Pet. Geol.* **2020**, *111*, 735–764. [CrossRef]
10. Yamamoto, K.; Boswell, R.; Collett, T.S.; Dallimore, S.R.; Lu, H. Review of past gas production attempts from subsurface gas hydrate deposits and necessity of Long-term production testing. *Energy Fuels* **2022**, *36*, 5047–5062. [CrossRef]
11. Collett, T.S.; Boswell, R.; Waite, W.F.; Kumar, P.; Roy, S.K.; Chopra, K.; Singh, S.K.; Yamada, Y.; Tenma, N.; Pohlman, J.; et al. India national gas hydrate program expedition 02 summary of scientific results: Gas hydrate systems along the eastern continental margin of India. *Mar. Pet. Geol.* **2019**, *108*, 39–142. [CrossRef]
12. Collett, T.S.; Zyrianova, M.V.; Okinaka, N.; Wakatsuki, M.; Boswell, R.; Marsteller, S.; Minge, D.; Crumley, S.; Itter, D.; Hunter, R.; et al. Planning and operations of the hydrate 01 stratigraphic test well, prudhoe bay unit, Alaska north slope. *Energy Fuels* **2022**, *36*, 3016–3039. [CrossRef]
13. White, M.D.; Kneafsey, T.J.; Seol, Y.; Waite, W.F.; Uchida, S.; Lin, J.S.; Myshakin, E.M.; Gai, X.; Gupta, S.; Reagan, M.T.; et al. An international code comparison study on coupled thermal, hydrologic and geomechanical processes of natural gas hydrate-bearing sediments. *Mar. Pet. Geol.* **2020**, *120*, 104566. [CrossRef]
14. Leclaire, P.; Cohen-Tenooudji, F.; Puente, J. Extension of Biot's theory of wave propagation to frozen porous media. *J. Acoust. Soc. Am.* **1994**, *96*, 3753–3768. [CrossRef]
15. Carcione, J.M.; Seriani, G. Wave simulation in frozen porous media. *J. Comput. Phys.* **2001**, *170*, 676–695. [CrossRef]
16. Liu, L.; Zhang, X.; Wang, X. Theoretical analysis and numerical simulation of acoustic waves in gas hydrate-bearing sediments. *Chin. Phys. B* **2021**, *30*, 024301. [CrossRef]
17. Shankar, U.; Riedel, M. Gas hydrate saturation in the Krishna-Godavari basin from P-wave velocity and electrical resistivity logs. *Mar. Pet. Geol.* **2011**, *28*, 1768–1778. [CrossRef]
18. Gao, H.Y.; Zhong, G.F.; Liang, J.Q.; Guo, Y. Estimation of gas hydrate saturation with modified Biot-Gassmann theory: A case from northern south China sea. *Mar. Geol. Quat. Geol.* **2012**, *32*, 83–89. [CrossRef]
19. Lee, M.W. Modified Biot-Gassmann theory for calculating elastic velocities for unconsolidated and consolidated sediments. *Mar. Geophys. Res.* **2002**, *23*, 403–412. [CrossRef]
20. Lin, L.; Liang, J.; Guo, Y.Q.; Lu, J.A.; Liang, J.Q. Estimating saturation of gas hydrates within marine sediments using sonic log data. *Well Logging Technol.* **2014**, *38*, 234–238.
21. Ecker, C.; Dvorkin, J.; Nur, A. Sediments with gas hydrates: Internal structure from seismic AVO. *Geophysics* **1998**, *63*, 1659–1669. [CrossRef]
22. Lee, M.W.; Waite, W.F. Estimating pore-space gas hydrate saturations from well log acoustic data. *Geochem. Geophys. Geosyst.* **2008**, *9*, Q07008. [CrossRef]
23. Zhang, R.W.; Li, H.Q.; Wen, P.F.; Zhang, B.J. The velocity dispersion and attenuation of marine hydrate-bearing sediments. *Chin. J. Geophys.* **2016**, *59*, 3417–3427.
24. Ecker, C.; Dvorkin, J.; Nur, A.M. Estimating the amount of gas hydrate and free gas from marine seismic data. *Geophysics* **2000**, *65*, 565–573. [CrossRef]
25. Liu, L.; Zhang, X.; Wang, X. Wave propagation characteristics in gas hydrate-bearing sediments and estimation of hydrate saturation. *Energies* **2021**, *14*, 804. [CrossRef]
26. Biot, M.A. Theory of propagation of elastic waves in a fluid-saturated porous solid, I-low frequency range. *J. Acoust. Soc. Am.* **1956**, *28*, 168–178. [CrossRef]
27. Biot, M.A. Theory of propagation of elastic waves in a fluid-saturated porous solid, II-higher-frequency range. *J. Acoust. Soc. Am.* **1956**, *28*, 179–191. [CrossRef]
28. Kvenvolden, K.A. Gas hydrates–geological perspective and global change. *Rev. Geophys.* **1993**, *31*, 173–187. [CrossRef]
29. Waite, W.F.; Santamarina, J.C.; Cortes, D.D.; Dugan, B.; Espinoza, D.N.; Germaine, J.; Jang, J.; Jung, J.W.; Kneafsey, T.J.; Shin, H.; et al. Physical properties of hydrate-bearing sediments. *Rev. Geophys.* **2009**, *47*, 1–38. [CrossRef]
30. Guerin, G.; Goldberg, D. Modeling of acoustic wave dissipation in gas hydrate-bearing sediments. *Geochem. Geophys. Geosyst.* **2005**, *6*, 1–16. [CrossRef]
31. Matsushima, J. Seismic Wave attenuation in methane hydrate-bearing sediments vertical seismic profiling data from the NankaiTrough exploratory well, offshore Tokai, central Japan. *J. Geophys. Res. Solid Earth* **2006**, *111*, 1–20. [CrossRef]
32. Guerin, G.; Goldberg, D. Sonic waveform attenuation in gas hydrate-bearing sediments from the Mallik 2L-38 research well, Mackenzie Delta, Canada. *J. Geophys. Res. B Solid Earth* **2002**, *107*, EPM-1. [CrossRef]

33. Matsushima, J. Attenuation measurements from sonic waveform logs in methane hydrate-bearing sediments at the Nankai Trough exploratory well off Tokai, central Japan. *Geophys. Res. Lett.* **2005**, *32*, 1–5. [CrossRef]
34. Liu, L.; Zhang, X.; Wang, X. Acoustic wave propagation in a borehole with a gas hydrate-bearing sediment. *J. Mar. Sci. Eng.* **2022**, *10*, 235. [CrossRef]
35. Chang, L. Study on Extracting Attenuation and Permeability of Anisotropic Reservoir from Acoustic Dipole Logging Data. Ph.D. Thesis, Jilin University, Jilin, China, 2009.
36. Tang, X.; Patterson, D.J. Mapping formation radial shear-wave velocity variation by a constrained inversion of borehole flexural-wave dispersion data. *Geophysics* **2010**, *6*, E183–E190. [CrossRef]
37. Xu, S.; Tang, X.; Su, Y.; Zhuang, C. Determining formation shear wave transverse isotropy jointly from borehole Stoneley- and flexural-wave data. *Chin. J. Geophys.* **2018**, *61*, 5105–5114.
38. Liu, L.; Zhang, X.; Wang, X.; He, X.; Chen, H. Component wave calculation and analysis of the acoustic field in a borehole within a three-phase porous medium. *Sci. Rep.* **2023**, *13*, 7646. [CrossRef]
39. Cheng, C.; Toksöz, M.N.; Willis, M.E. Determination of in situ attenuation from full waveform acoustic logs. *J. Geophys. Res.* **1982**, *87*, 5477–5484. [CrossRef]